IVYSPRING INTERNATIONAL PUBLISHER

Theranostics

2027; 17(1): 627-645. doi: 10.7150/thno.142353

Research Paper

Piezocatalytic microneedle platform for biocompatible and antibacterial ROS therapy of infected wounds

Zesheng Chen[1,2*], Fanghan Li[2*], Wenwen Cheng[2], Ye Yang[2], Zhengyao Zhang[3], Wang Wang[1], Weikang Hu[2*], Weijun Liu[4✉], Zijian Wang[1,3✉]

1. Department of Urology, Hubei Key Laboratory of Urological Diseases, Institute of Urology, Zhongnan Hospital of Wuhan University, Wuhan 430071, China.
2. Hubei Province Key Laboratory of Biotechnology of Chinese Traditional Medicine, College of Health Science and Engineering, Hubei University, Wuhan 430062, China.
3. Department of Biomedical Engineering, TaiKang Medical School (School of Basic Medical Sciences), Wuhan University, Wuhan 430071, China.
4. Department of Orthopedics Surgery, Renmin Hospital of Wuhan University, Wuhan 430060, China.

* These authors contributed equally to this work.

✉ Corresponding author: Department of Urology, Zhongnan Hospital of Wuhan University, Wuhan 430071, China. E-mail address: Zijianwang@whu.edu.cn (Z. Wang); Department of Orthopedics Surgery, Renmin Hospital of Wuhan University, Wuhan 430060, China E-mail address: iamliu2003@163.com (W. Liu).

© 2027 The Author(s). This is an open access article distributed under the Creative Commons Attribution 4.0 International Licence, subject to the Publisher's Terms of Use at https://ivyspring.com/terms.

Received: 2026.08.11; Accepted: 2026.10.08; Published: 2027.01.01

Abstract

Rationale: Reactive oxygen species (ROS) are emerging antibacterial molecules that exert antibacterial effects via multi-target attack on cell membranes, proteins, and DNA. However, ROS is a double-edged sword, as it can not only eliminate bacteria but also induce damage to mammalian cells. Achieving an optimal balance between ROS-mediated antibacterial efficacy and biocompatibility remains a challenge.

Methods: This study proposes a maltose (Mal)-mediated strategy for bacteria-specific ROS modulation. As a proof of concept, piezocatalytic Mal/$BaTiO_3$ composite nanosheets (namely MBT) are prepared via a two-step reaction. A bilayer gelatin methacryloyl/MBT composite microneedle (namely MBTM) is further fabricated to deliver MBT into skin wounds. The selective internalization of MBT by bacteria, intracellular ROS levels, antibacterial activity, biocompatibility, and wound healing in *S. aureus*-infected wounds are comprehensively evaluated.

Results: MBT nanosheets are successfully prepared. They can be selectively internalized by bacteria, leading to elevated intracellular ROS levels and subsequent bacterial death, without exerting detrimental effects on mammalian cells. The fabrication of MBTM microneedle reduces the required dosage of MBT and minimizes potential adverse effects. MBTM microneedle possesses both biocompatibility and broad-spectrum antibacterial activity, and accelerates *S. aureus*-infected wound healing via complex mechanisms.

Conclusions: This study not only establishes a Mal-mediated bacteria-specific ROS modulation strategy but also provides a piezocatalytic microneedle platform that integrates selective antibacterial activity with biocompatibility for infected wound management.

Keywords: wound healing, microneedle, piezoelectric, ROS, antibacterial

Introduction

Chronic cutaneous wounds resulting from trauma, burns, surgical incisions, or diabetes mellitus pose a growing disease burden that demands urgent attention [1]. Bacterial infection is one of the major obstacles to wound healing, accounting for complications in 30-60% of clinical cases [2]. In the past decades, antibiotics, although aimed at combating bacterial infections, have contributed to the rise of antimicrobial resistance. Their applications are further limited by a narrow activity spectrum, hypersensitivity, adverse toxicity, and excessive prescribing [3, 4]. As a result, alternative strategies to conventional antibiotics are increasingly being pursued.

Reactive oxygen species (ROS), including superoxide anion ($\cdot O_2^-$), hydroxyl radical (OH),

hydrogen peroxide (H_2O_2), and singlet oxygen ($^1O_2$) are emerging antibacterial molecules [5, 6]. ROS exerts its antibacterial effects via multi-target attack on bacterial cell membranes, proteins, DNA, and metabolism [7]. Compared with other antibacterial strategies, ROS offers several distinct advantages, including high efficacy, broad-spectrum activity and stimuli-responsive behaviors [8]. Micro/nano materials are capable of inducing ROS formation through piezocatalytic or photocatalytic processes. [9-11]. For example, Shi et al. reported a bionic cooling skin loaded with single-sided metal-organic frameworks (MOFs) for visible light-responsive ROS generation and broad-spectrum antibacterial treatment [12]. Xu et al. also reported a piezoelectric bandage incorporating ultrasmall $BaTiO_3$ (BTO) nanoparticles for ROS generation, which eradicated over 90% of *S. aureus* within 10 min and achieved 92.6% wound closure in 14 days [13]. These favorable results fully demonstrate the prospects of ROS for antibacterial wound healing applications.

To date, considerable efforts have been devoted to developing ROS-producing nano-micro materials, with significant progress in materials design and composite engineering that has markedly enhanced their antibacterial efficiency [14-16]. However, ROS acts as a double-edged sword, as it can likewise induce oxidative injury to mammalian cells. The optimal balance between ROS-mediated antibacterial efficacy and biocompatibility remains elusive.

To address this problem, this study first proposes a maltose (Mal)-mediated strategy for bacteria-specific ROS modulation. The metabolic profiles of bacteria and mammalian cells differ markedly [17]. To fuel their active metabolism, most bacteria are capable of taking up environmental Mals, including maltose, maltotriose, and maltohexaose, through several mechanisms including an adenosine 5'-triphosphate-binding cassette (ABC) pathway [18-20]. However, mammalian cells are deficient in this function and cannot internalize the Mal [21]. Thus, Mal can serve as a targeted delivery vehicle to selectively transport ROS-generating nanomaterials into bacterial cells, while sparing mammalian cells and enabling spatiotemporally controlled ROS generation within bacteria. This study further develops a Mal-modified BTO nanosheets as a proof-of-concept. As shown in Figure 1A, piezocatalytic BTO nanosheets are synthesized via a hydrothermal method, and subsequently coated with a Mal layer through a solvothermal process to yield Mal /BTO (namely MBT) composite nanosheets. Owing to the Mal coating, MBT nanosheets are selectively internalized by bacteria, leading to elevated intracellular ROS levels and subsequent bacterial death. Meanwhile, MBT nanosheets will not exert any detrimental effects on human cells.

MBT nanosheets, like many other nanomaterials, suffer from inherent drawbacks such as a tendency to aggregate, insufficient biodegradability, and suboptimal drug delivery capabilities, all of which impede their application potential for wound healing [22, 23]. Biomolecular microneedles, composed of micron-scale tip arrays, serve as a minimally invasive and biocompatible platform for transdermal drug delivery [24]. Through rational design of their raw materials, architecture, and release kinetics, biomolecular microneedles can achieve programmed, spatiotemporally controlled drug delivery [25, 26]. Thus, they represent an ideal candidate for modifying the MBT nanosheets. As shown in Figure 1B, this study also fabricates a bilayer microneedle platform via a mold-casting technique. The base layer was composed of a gelatin methacryloyl (GelMA) matrix, while the tip layer was loaded with MBT nanosheets. It is hypothesized that the MBTM microneedle platform can precisely deliver MBT nanosheets into skin wounds, thereby reducing the required dosage and minimizing potential adverse effects.

In this study, the physicochemical properties, ROS-generating capacity, biocompatibility, broad antibacterial action and wound repair ability of MBT nanosheets and MBTM microneedles will be systematically evaluated. As shown in Figure 1C, MBTM microneedles are hypothesized to combine biocompatibility with bioactivity to promote cell migration, along with broad-spectrum antibacterial activity to suppress bacterial survival and proliferation. Furthermore, MBTM microneedles are expected to accelerate infected wound healing through multifaceted mechanisms. In conclusion, this study will not only establish a Mal-mediated bacteria-specific ROS modulation strategy, but also provide a piezocatalytic microneedle platform that integrates highly selective antibacterial activity with biocompatibility for infected wound management.

Results and Discussion

MBT nanosheets were fabricated via a two-step method

In this study, BTO nanosheets were initially synthesized via a hydrothermal method and subsequently coated with a Mal layer through a solvothermal process to yield MBT nanosheets. Figure 2A-B show the results of transmission electron microscopy (TEM) observation. BTO nanosheets exhibited an ultrathin morphology, with individual sheets having a lateral size of approximately 5 nm. The lattice fringe spacing of BTO is approximately 0.28 nm,

corresponding to the (101) crystal plane [27]. The outer surface of the MBT nanosheets was coated with a Mal layer (marked in blue). MBT exhibited a lattice spacing of 0.28 nm, indicating that the BTO crystal structure was preserved after the solvothermal treatment. The lateral size of the MBT nanosheets is significantly smaller than 10 nm, which is much smaller than that of bacteria, implying that MBT can be internalized by bacterial cells. Figure 2C and Figure S1 show the TEM mapping of MBT and BTO, respectively. Compared with BTO nanosheets, MBT nanosheets exhibited stronger C signal. This phenomenon confirmed the coating of Mal layer.

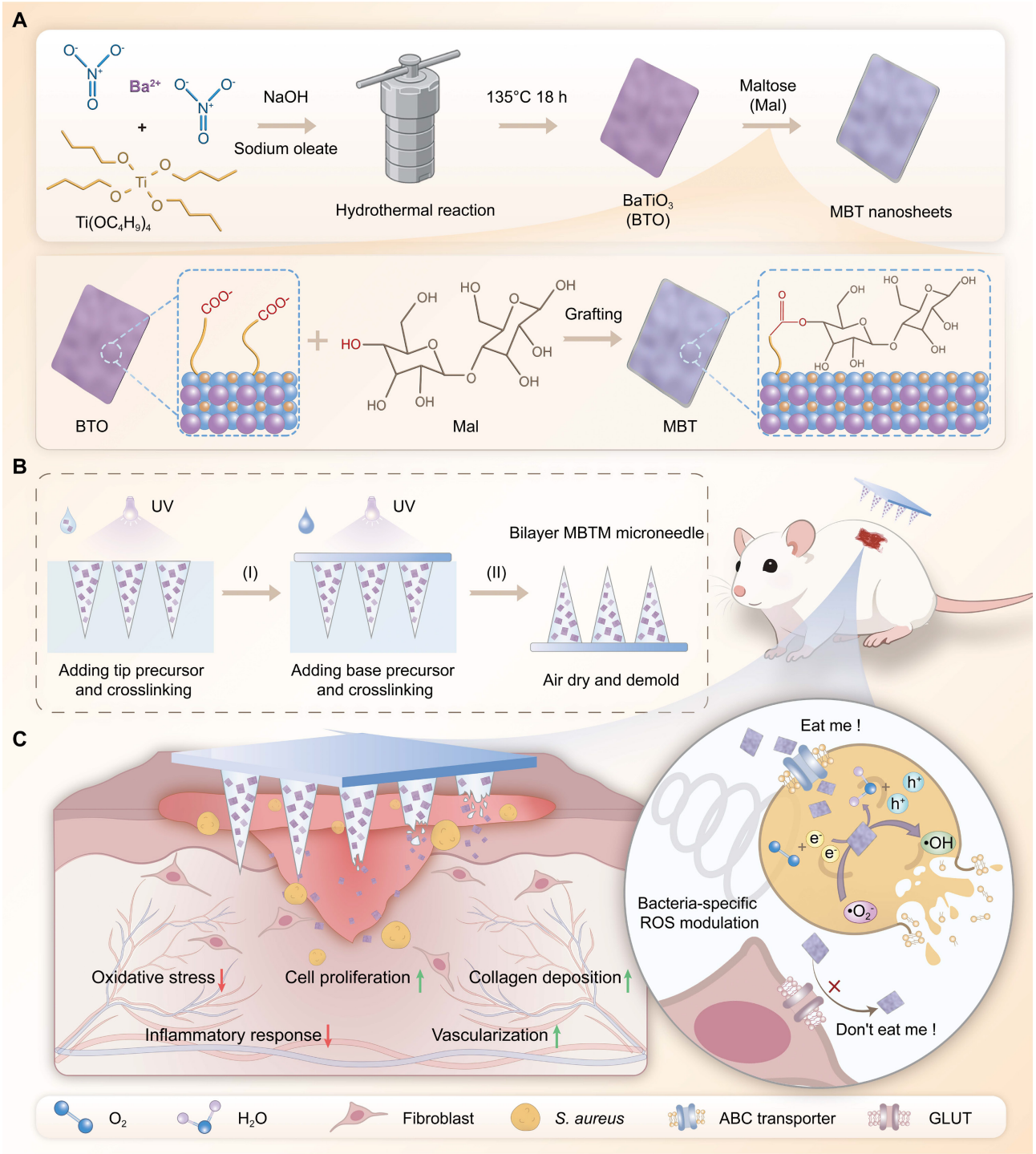


Figure 1. Fabrication and biomedical applications of GBT nanosheets and composite microneedles. (A) MBT nanosheets were prepared via a two-step reaction, highlighting the covalent grafting between BTO nanosheets and Mal molecules; (B) Bilayer MBTM microneedles were fabricated using a mold-casting technique; (C) Upon ultrasound stimulation, MBTM microneedle achieves both excellent antibacterial efficacy and favorable biocompatibility through a Mal-mediated bacteria-specific ROS modulation strategy, and accelerates *S. aureus*-infected wound healing via complex mechanisms.

As shown in Figure 2D, the chemical composition of the MBT nanosheets was verified by Fourier transform infrared spectroscopy (FT-IR). The peak at 550 cm^{-1} was assigned to the stretching vibration of the Ti-O bond in BTO, indicating that the BTO structure was retained [28]. In the spectrum of BTO, the aliphatic $\nu(CH_2)$ bands at 2925 and 2851 cm^{-1}, together with the paired peaks at 1550 and 1450 cm^{-1} ascribed to $vas(COO^-)$ and $vs(COO^-)$, confirmed that the oleate ligand layer introduced during the hydrothermal synthesis was retained on the nanosheet surface, thereby providing the surface carboxyl groups required for the subsequent conjugation. The peak at 3420 cm^{-1} corresponded to the stretching vibration of the -OH groups of Mal. Upon grafting, MBT exhibited intense absorptions in the 1200-1000 cm^{-1} region, including that at 1055 cm^{-1}, which were absent in the spectrum of BTO and originated from the pyranose ring and glycosidic C-O-C/C-O-H vibrations of Mal, indicating that Mal had been successfully introduced onto the nanosheet surface. As Mal bears hydroxyl groups only and no carboxyl functionality, esterification between these hydroxyl groups and the free surface carboxyl groups is the only pathway by which the two components can be covalently linked under the DCC/DMAP conditions employed, and the reaction is expected to proceed preferentially at the sterically accessible primary hydroxyl (C6) sites. Moreover, the product was subjected to three washing cycles with DMF and then three with methanol, in both of which Mal is readily soluble, so that any residual physically adsorbed Mal would be negligible. Taken together, these results indicate that Mal was covalently grafted onto the carboxyl groups of the oleate ligand layer on the BTO surface via esterification, affording a Mal-functionalized surface layer. Figure 2E shows the results of X-ray diffraction (XRD). Both MBT and BTO exhibited characteristic peaks at 31°, 38°, 44°, and 55°, which correspond to the (101), (111), (200), and (211) planes of barium titanate, respectively. The lattice parameters of BTO and MBT were consistent, indicating that the Mal coating did not alter the inherent structure of the nanosheets.

Figure 2F shows the X-ray photoelectron spectroscopy (XPS) survey spectra of MBT. The characteristic peaks corresponding to Ba, O, Ti, and C have been marked in the spectra. Figure S2A-D show the high-resolution XPS spectra. The Ba 3d spectrum showed peaks at 793 eV ($3d_{3/2}$) and 778 eV ($3d_{5/2}$). The Ti 2p peaks were resolved into two components at 458 eV ($2p_{3/2}$) and 463 eV ($2p_{1/2}$). In the O 1s region, the peaks at 529 eV and 531 eV were attributable to Ba-O/Ti-O bonds in barium titanate and -OH groups in Mal, respectively [29, 30]. The C 1s peaks at 284 eV and 288 eV corresponded to C-C and O-C=O functionalities in the Mal coating. The results of FT-IR, XRD and XPS collectively confirmed that Mal layer was covalently conjugated to BTO nanosheets without altering their inherent structure.

As shown in Figure 2G, the Zeta potential was -21.73 ± 1.14 mV for BTO, -10.93 ± 0.57 mV for Mal, and -20.4 ± 1.45 mV for MBT, respectively. Both BTO and Mal were negatively charged. Thus, the electrostatic interactions were not involved in the reactions of this study. Figure 2H shows the thermogravimetric (TG) curves. BTO exhibited a low-temperature weight loss (~100°C) due to desorption of surface water, and a high-temperature weight loss (~400°C) arising from the decomposition of oleic acid. In the TG curve of MBT, an additional weight loss at around 270°C was observed, which was ascribed to the decomposition of the Mal coating. Based on these results, the Mal loading capacity of MBT was calculated to be approximately 3.24%.

In conclusion, core-shell MBT nanosheets were first prepared through a two-step strategy, in which BTO nanosheets constituted the core and Mal formed the shell. Mal was immobilized onto the outer surface of BTO by covalent crosslinking rather than electrostatic interaction. The obtained MBT nanosheets exhibited ultrasmall size less than 10 nm, enabling it to be internalized by bacterial cells. The Mal coating can confer high selectivity on the internalization process. However, the properties of MBT nanosheets in modulating the biological behaviors of bacterial cells remain to be investigated.

MBT nanosheets demonstrated piezoelectric properties

As a prototypical piezoelectric semiconductor, BTO exhibits piezoelectricity that stems from its non-centrosymmetric crystal lattice, with its semiconducting attributes playing a substantial role in modulating this response [31]. Under ultrasound stimulation, a piezoelectric field is generated inside BTO, which promotes electron–hole pair separation and induces a series of piezocatalytic reactions. By integrating material composites, defect engineering, and novel physical effects, researchers have steadily boosted the piezoelectric performance of BTO, unlocking its significant potential for biomedical applications [32]. In this study, BTO and Mal were integrated into one nanoplatform to fabricate composite MBT. The incorporation of BTO is hypothesized to endow MBT with desirable piezoelectric properties, which catalyzes ROS generation and thereby exerts potent bactericidal effects.

To verify this hypothesis, an electrochemical workstation was applied to characterize the

piezoelectric performance of MBT. Figure 2I shows the results of piezoresponse force microscopy (PFM). The bias voltage was swept from -10 V to 10 V. MBT nanosheets demonstrated a typical butterfly amplitude curve with 180° phase switching, indicative of their piezoelectricity and polarization switching behavior [33]. Electrochemical impedance spectroscopy (EIS) and i-t curve data are provided in Figure 2J-K, respectively. The insulating effect of Mal layer resulted in a slightly higher impedance for MBT compared with BTO. Nevertheless, the impedance of MBT remained relatively low, suggesting efficient electron migration under ultrasound stimulation. Both BTO and MBT exhibited high current densities in the i-t curves upon ultrasound stimulation. Collectively, these results validated our hypothesis that MBT possesses desirable piezoelectric properties.

MBT triggered ROS generation under ultrasound stimulation

The ROS generation capability of MBT nanosheets was comprehensively investigated *in vitro*. 3,3',5,5'-tetramethylbenzidine (TMB) assay was performed to detect ·OH. As shown in Figure 2L-N, colorless TMB reacts with ·OH to form blue Ox-TMB under ultrasound stimulation, which exhibits a characteristic absorption peak at 652 nm [34]. Compared to other groups, MBT group showed a significantly higher peak intensity, implying more efficient ·OH production. Meanwhile, MBT modulated ·OH generation in a dose- and time-dependent manner. The results of TMB assay were further confirmed by electron paramagnetic resonance (EPR) assay (Figure 2O). Both the BTO and MBT groups exhibited a typical 1:2:2:1 quartet characteristic peak of ·OH after ultrasound treatment, confirming the ·OH production. As shown in Figure 2P-R, nitroblue tetrazolium (NBT) assay was performed to detect $\cdot O_2^-$. The results demonstrated that MBT catalyzes $\cdot O_2^-$ generation as effectively as BTO. As shown in Figure 2S, $\cdot O_2^-$ was also detected by EPR assay. MBT group exhibited a characteristic six-line signal, further confirming the $\cdot O_2^-$ generation.

In conclusion, MBT nanosheets combined with ultrasound treatment generated both ·OH and $\cdot O_2^-$ in a dose- and time-dependent manner. MBT nanosheets can generate electron-hole pairs under ultrasound excitation. The conduction band electrons reduce O_2 to $\cdot O_2^-$, while the valence band holes oxidize H_2O/OH- to ·OH. They both are key ROS that strongly oxidize bacterial structures, rarely trigger resistance, and offer a promising solution for the post-antibiotic era. However, the non-specific reactivity of ROS enables their action against both bacterial pathogens and mammalian cells, creating a therapeutically beneficial yet intrinsically toxic paradox. Hence, the development of strategies to enhance antibacterial selectivity while circumventing oxidative damage constitutes a critical priority for ongoing investigations.

MBT were selectively internalized by bacterial cells

In recent years, researchers have exploited bacteria to actively take up Mals, thereby enabling delivery of small molecules/nanomaterials into bacteria [18-20]. This biological behavior is not observed in mammalian cells. Thus, Mal with good biocompatibility and cellular recognition capabilities, emerges as a promising solution to achieve bacterial-target delivery of MBT nanosheets, bacteria-specific ROS modulation, and enhanced antibacterial efficiency, while avoiding oxidative stress damage to normal tissue. In this study, it is hypothesized that the Mal layer confers high selective uptake by bacteria on MBT nanosheets and enables targeted ROS burst inside bacterial cells.

As shown in Figure 3A, both gram-positive *S. aureus* and gram-negative *E. coli* bacteria were cultured with MBT nanosheets. After ultrasound treatment, a series of wet assays were performed. Figure 3B-C shows the TEM images. High-density nanoparticle structures were detected in the MBT group but were undetectable in the BTO group. Notably, the intracellular biodistribution of MBT nanosheets has been marked with red arrows. These results confirmed that MBT nanosheets can be internalized by both *S. aureus* and *E. coli*. Figure 3D-E shows the results of fluorescence tracking. Fluorescein 5-isothiocyanate (FITC)-labeled MBT nanosheets were cultured with bacteria and L929 cells at the same time. After ultrasound treatment, only bacteria cells were fluorescently labeled with green, whereas the L929 cells were not. These results further confirmed that MBT nanosheets can be selectively internalized by *S. aureus* and *E. coli*.

MBT upregulated intracellular ROS level in bacteria

ROS can be divided into extracellular and intracellular types, which differ markedly in their action pathways and mechanisms [35, 36]. This study has confirmed that MBT nanosheets can be selectively internalized by bacteria. However, the role of intracellular MBT nanosheets in modulating ROS remains to be uncovered.

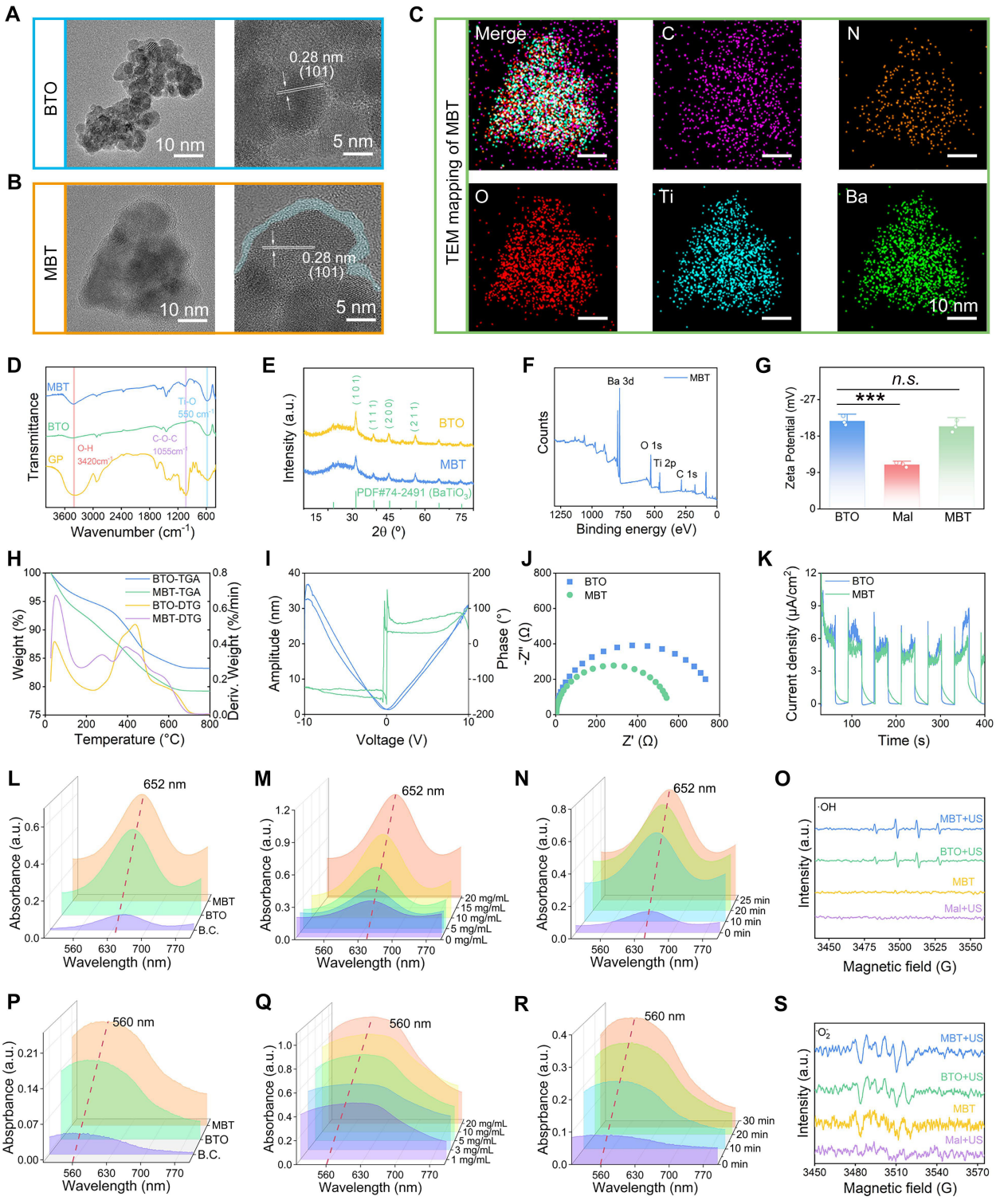


Figure 2. Piezocatalytic MBT nanosheets were fabricated for burst ROS generation. (A-B) TEM images of BTO and MBT. Scale bars: 10 nm and 5 nm; (C) TEM energy-dispersive mapping of MBT. Scale bar: 10 nm; (D) FT-IR spectrum; (E) XRD patterns; (F) XPS survey spectra; (G) Zeta potential (n = 3 biological replicates); (H) TG analysis; (I) PFM images; (J) EIS plots; (K) I-t curves; (L-N) UV-vis analysis for TMB assay; (O) EPR spectrum for detecting ·OH; (P-R) UV-vis analysis for NBT assay; (S) EPR spectrum for detecting $\cdot O_2^-$. All values are presented as mean ± SD. Statistical significance was assessed by one-way ANOVA. In inter-group comparisons, *n.s.* indicates no significance, ***$P < 0.001$.

As shown in Figure 3F, Figure 3I and Figure S3, the intracellular ROS levels of both *E. coli* and *S. aureus* were detected using a DCFH-DA probe. The quantitative results of fluorescence intensity revealed that MBT nanosheets combined with ultrasound treatment (MBT+US group) efficiently upregulated the ROS level. Compared to other groups, statistically significant differences were detected ($P < 0.001$).

Notably, the BTO+US group also showed elevated intracellular ROS levels, attributed to BTO-induced changes in the intracellular microenvironment that triggered bacterial oxidative stress and subsequent ROS accumulation. As shown in Figure 3G-H and Figure 3J-K, MBT+US could also increase the content of intracellular malondialdehyde (MDA), while decreased the content of intracellular glutathione (GSH). Compared to other groups, significant differences were observed ($P < 0.05$).

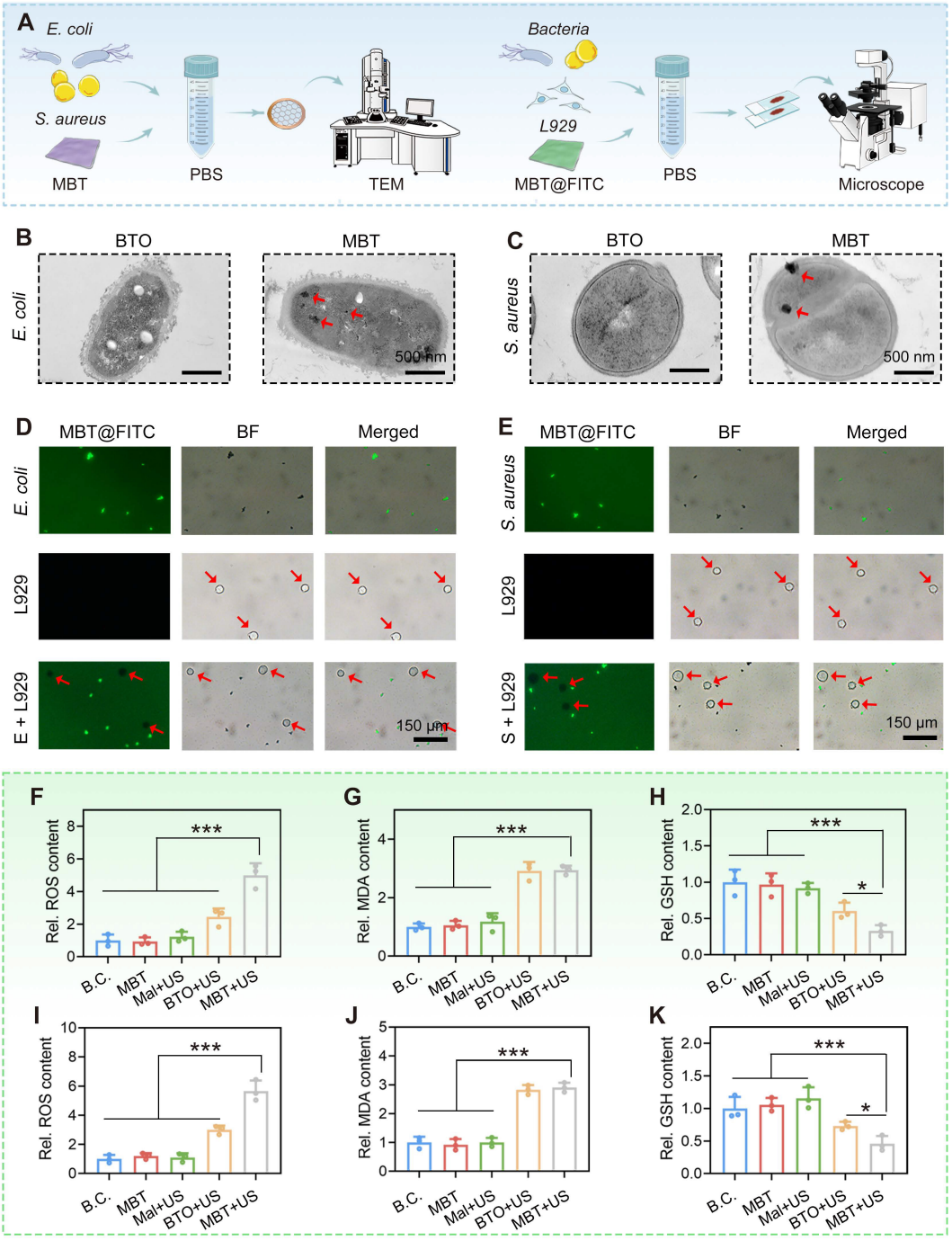


Figure 3. The Mal layer conferred selective antibacterial potential onto MBT nanosheets. (A) A diagram showing the experimental protocols; (B) TEM images of *E. coli* co-cultured with BTO and MBT nanosheets. Scale bar: 500 nm; (C) TEM images of *S. aureus*. Scale bar: 500 nm; (D) Fluorescence images of FITC-labeled MBT co-cultured with *E. coli* and L929 cells (L929 cells are marked with red arrows). Scale bars: 150 μm; (E) Fluorescence images of FITC-labeled MBT co-cultured with *S. aureus* and L929 cells (L929 cells are marked with red arrows). Scale bars: 150 μm; (F-H) Quantitative analysis of intracellular ROS, MDA, and GSH levels in *E. coli*, respectively (n = 3 biological replicates); (I-K) Quantitative analysis of intracellular ROS, MDA, and GSH levels in *S. aureus*, respectively (n = 3 biological replicates). All values are presented as mean ± SD. Statistical significance was assessed by one-way ANOVA. In inter-group comparisons, *$P < 0.05$, ***$P < 0.001$.

In conclusion, this study confirmed that MBT nanosheets can be selectively internalized by both *S. aureus* and *E. coli* to upregulate their intracellular ROS levels, exhibiting preliminary potential for broad-spectrum antibacterial and wound healing applications. However, like most nanomaterials, MBT nanosheets suffer from issues such as aggregation propensity, poor biodegradability, and drug delivery hurdles, which constrain their application in wound healing. Developing composite biomaterials to overcome these limitations remains a significant challenge.

MBT was modified by GelMA hydrogels

MBT nanosheets were modified with GelMA hydrogels to overcome their inherent limitations. As illustrated in Figure 4A, four MBTH-n hydrogel formulations were fabricated by varying the MBT nanosheet loading. MBTH-0 was formulated using only pristine 15% GelMA, while the remaining formulations (MBTH-0.2, 0.5, and 0.8) were supplemented with escalating dosages of MBT nanosheets. After UV crosslinking, all samples transformed from liquid into solid, indicating the formation of a crosslinked GelMA network. Notably, MBT nanosheets did not participate in the chemical crosslinking process. Instead, they were physically dispersed and embedded in the GelMA network, thereby retaining their bioactivity to the maximum extent.

To characterize the MBTH-n hydrogels, a series of physicochemical tests were conducted. As shown in Figure 4B, all MBTH-n hydrogels exhibited a typical porous sponge-like structure, owing to the phase separation upon freeze-drying [37]. The pore size increased gradually as the MBT content increased, which is beneficial for gas supply, maintaining a moist environment, and absorbing wound exudates. As shown in Figure 4C-D, the water contact angle of MBTH-n hydrogels was detected. It was 91.52 ± 1.97° for MBTH-0, 86.02 ± 1.72° for MBTH-0.2, 82.83 ± 1.06° for MBTH-0.5, and 80.23 ± 0.25° for MBTH-0.8, respectively. MBT significantly enhanced the hydrophilicity of composite hydrogels ($P < 0.01$), which was likely due to hydrogen bonds formed between Mal hydroxyl groups and water [38]. As shown in Figure 4E, MBTH-0.8 hydrogel exhibited the fastest water absorption rate and highest water uptake among four groups, owing to its larger pore size, porosity as well as the increased hydrophilicity conferred by MBT. Figure 4F-G displays the compression test results, which indicate a gradual reduction in the elastic modulus of MBTH-n hydrogels as the MBT content rose.

In conclusion, the incorporation of MBT modulated the pore size, hydrophilicity, swelling ability, and mechanical strength of MBTH-n hydrogels in a dose-dependent manner. Based on these results, MBTH-0.5 hydrogel was selected for subsequent microneedle patch fabrication, as it retains sufficient mechanical strength to accommodate microneedle insertion and skin conformity, while also exhibiting significantly improved hydrophilicity and swelling capacity.

Bilayer MBTM microneedle was fabricated by mold-casting

MBTH-0.5 hydrogel was processed into microneedle patches to enhance the delivery efficiency of MBT nanosheets to wounds. In accordance with our previous report [39], this study adopts a bilayer design of MBTM microneedle. MBTH-0 hydrogel served as the base layer, while the tip layer was formed from MBTH-0.5 hydrogel. This bilayer design not only reduced the dosage of MBT nanosheets, but also alleviated its potential adverse effects, such as hyperpigmentation.

MBTM microneedle was fabricated using a mold-casting technique. As shown in Figure 4H-I, both GM (neat GelMA microneedle) and MBTM exhibited a typical microneedle array. The tips of the MBTM microneedle were white due to the MBT nanosheets, whereas the base layer, consisting of pure GelMA, was light yellow. Compared to pristine GM microneedle, the tips of MBTM exhibited a rougher surface. Collectively, these results confirmed the successful fabrication of bilayer MBTM microneedle. As shown in Figure S4, the maximum force per tip was 0.170 N for GM microneedles and 0.143 N for MBTM microneedles, both exceeding the reported skin penetration threshold of 0.098 N [40]. As shown in Figure 4J, MBTM microneedle could penetrate the skin of BALB/c nude mice, which is consistent with our previous report [41]. The skin puncturing capability of MBTM microneedles is mainly attributed to the rigid GelMA microneedle structure, allowing for transdermal delivery of MBT nanosheets. Once drug delivery is complete, the tips composed of GelMA hydrogels can rapidly degrade without leading to potential side effects. MBT nanosheets will remain *in vivo* for a longer duration. Thus, a single administration is sufficient to achieve sustained therapeutic efficacy, with favorable prospects for clinical translation.

As shown in Figure S5A-B and Figure S6, Rhodamine B (Rh. B) was used as a fluorescent probe to assess the release behavior of MBTM microneedles. The results indicated that MBTM microneedle rapidly released the Rh. B loaded in the tips within the first 2 h, with the release plateauing at 12 h. Such a rapid and

plateau-reaching release profile suggests efficient cargo discharge upon skin penetration. Accordingly, when applied to wounds *in vivo*, MBTM microneedle is capable of swiftly liberating their payload, including MBT nanosheets, into the underlying skin tissue to exert therapeutic effects.

MBTM demonstrated good biocompatibility and bioactivity

To examine the biocompatibility of MBTM microneedles *in vitro*, L929 cells were used as a cell model and co-cultured with the microneedles. The MTT assay results are presented in Figure S7. Compared with the blank control (B.C.) group, the cell viability in the MBTM and MBTM+US groups showed no significant difference ($P > 0.05$). This phenomenon suggested that MBTM, either alone or combined with ultrasound, exhibited favorable cytocompatibility. Specifically, MBT nanosheets released from MBTM microneedles do not enter L929 cells, nor do they induce intracellular ROS upregulation. As shown in Figure 4K-L, the cell viability was further validated by live/dead cell staining assay. Live cells were dyed green, while dead cells were dyed red. The majority of L929 cells in both the MBTM and MBTM+US groups exhibited green fluorescence, confirming good cytocompatibility.

As illustrated in Figure 4M-N, L929 cell migration was assessed by a scratch assay. Following 24 h of co-culture, the migration rates reached 29.99 ± 1.87% for B.C. group, 35.69 ± 3.07% for GM group, 43.02 ± 3.07% for MBTM group and 47.69 ± 1.54% for MBTM+US group, respectively. Compared with B.C. group, MBTM and MBTM+US groups showed significantly enhanced cell migration ability ($P < 0.001$), partially owing to the vital role of Mal coating on the MBT nanosheets. This finding is consistent with the report by Brash et al., who demonstrated that a structurally tailored Mal improves cell migration and endothelialization of materials [42]. The enhanced cell migration observed in this study is expected to actively promote wound healing. In conclusion, MBTM microneedle has demonstrated good biocompatibility and bioactivity, making it a promising candidate for wound healing applications.

MBTM demonstrated broad-spectrum antibacterial activity

As shown in Figure 3, our results have revealed that MBT nanosheets can be selectively internalized by both *S. aureus* and *E. coli* to up regulate their intracellular ROS levels, suggesting preliminary broad-spectrum antibacterial potential. As shown in Figure 4, MBT nanosheets were further modified with GelMA hydrogel to fabricate a composite MBTM microneedle material. In this study, it was hypothesized that incorporating MBT nanosheets would confer enhanced broad-spectrum antibacterial activity on the MBTM microneedle. However, this hypothesis has yet to be experimentally validated.

Herein, the antibacterial effects of MBTM microneedles against a broad range of bacteria were systematically investigated. Bacterial viability was determined by a plate clone assay, with the results shown in Figure 5A-C. The results demonstrated that BTOM and MBTM significantly inhibited the survival ability of both *E. coli* and *S. aureus* under ultrasound stimulation ($P < 0.001$). The bacterial proliferation curves in Figure 5D-E further indicated that BTOM and MBTM suppressed bacterial proliferation under ultrasound stimulation. As shown in Figure S8, BTOM+US and MBTM+US also exhibited good antibacterial activity against Methicillin-resistant *Staphylococcus aureus* (MRSA). To further assess bacterial viability, SEM observation and live/dead bacterial staining assay were performed. Figure 5F shows the results of SEM observation. BTOM and MBTM disrupted the bacterial cell membranes upon ultrasound exposure, leading to the collapse of bacterial bodies. Figure 5G-I show the results of live/dead bacterial staining assay. Extensive bacterial death was observed in both the BTOM+US and MBTM+US groups. As shown in Figure S9, the antibacterial activity of MBTM+US was effectively rescued by vitamin E, confirming that the antibacterial effect is specifically mediated by ROS. Notably, the antibacterial mechanism of BTOM+US was attributed to extracellular ROS, while that of MBTM+US was attributed to intracellular ROS. They were fundamentally different [7]. Specifically, extracellular ROS oxidize cell membrane components and disrupt the membrane structure, thereby exerting antibacterial effects through chemical and physical mechanisms. Intracellular ROS participate in the regulation of cellular homeostasis and kill bacteria through biological pathways such as amplifying oxidative stress damage. Collectively, these results confirmed that MBTM exhibits potent broad-spectrum antibacterial activity, comparable to that of the penicillin-positive control, suggesting that MBTM microneedles are a promising biomaterial for wound infection therapy.

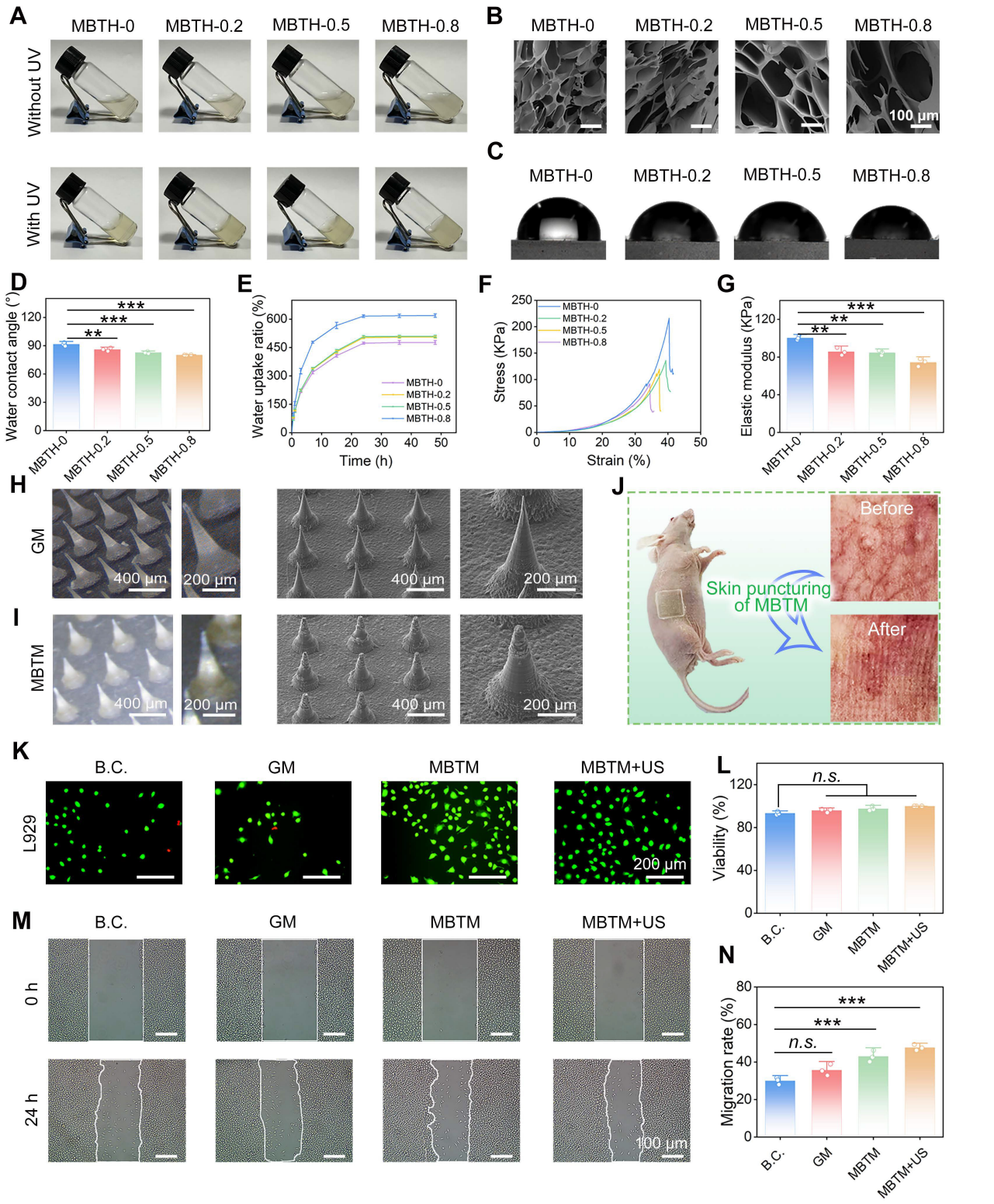


Figure 4. MBT-laden microneedle was fabricated with enhanced drug delivery capability and good biocompatibility. (A) The gelation process of MBTH-n hydrogels; (B) SEM images revealing the architecture of MBTH-n hydrogels after freeze-drying. Scale bar: 100 μm; (C-D) Water contact angle test (n = 3 biological replicates); (E) Water absorption ratio of the hydrogels (n = 3); (F) Representative stress-strain curves; (G) Elastic modulus (n = 3 biological replicates); (H-I) Optical and SEM images of GM and MBTM microneedles. Scale bar: 400 and 200 μm; (J) Optical image of MBTM microneedle piercing the skin of nude mice; (K) Live/dead staining images of L929 cells. Scale bar: 200 μm; (L) Quantitative results of live/dead cell staining (n = 3 biological replicates); (M) Scratch assay of L929 cells. Scale bar: 200 μm; (N) Quantitative results of cell migration (n = 3 biological replicates). All values are presented as mean ± SD. Statistical significance was assessed by one-way ANOVA. In inter-group comparisons, *n.s.* indicates no significance, **P* < 0.05, ****P* < 0.001.

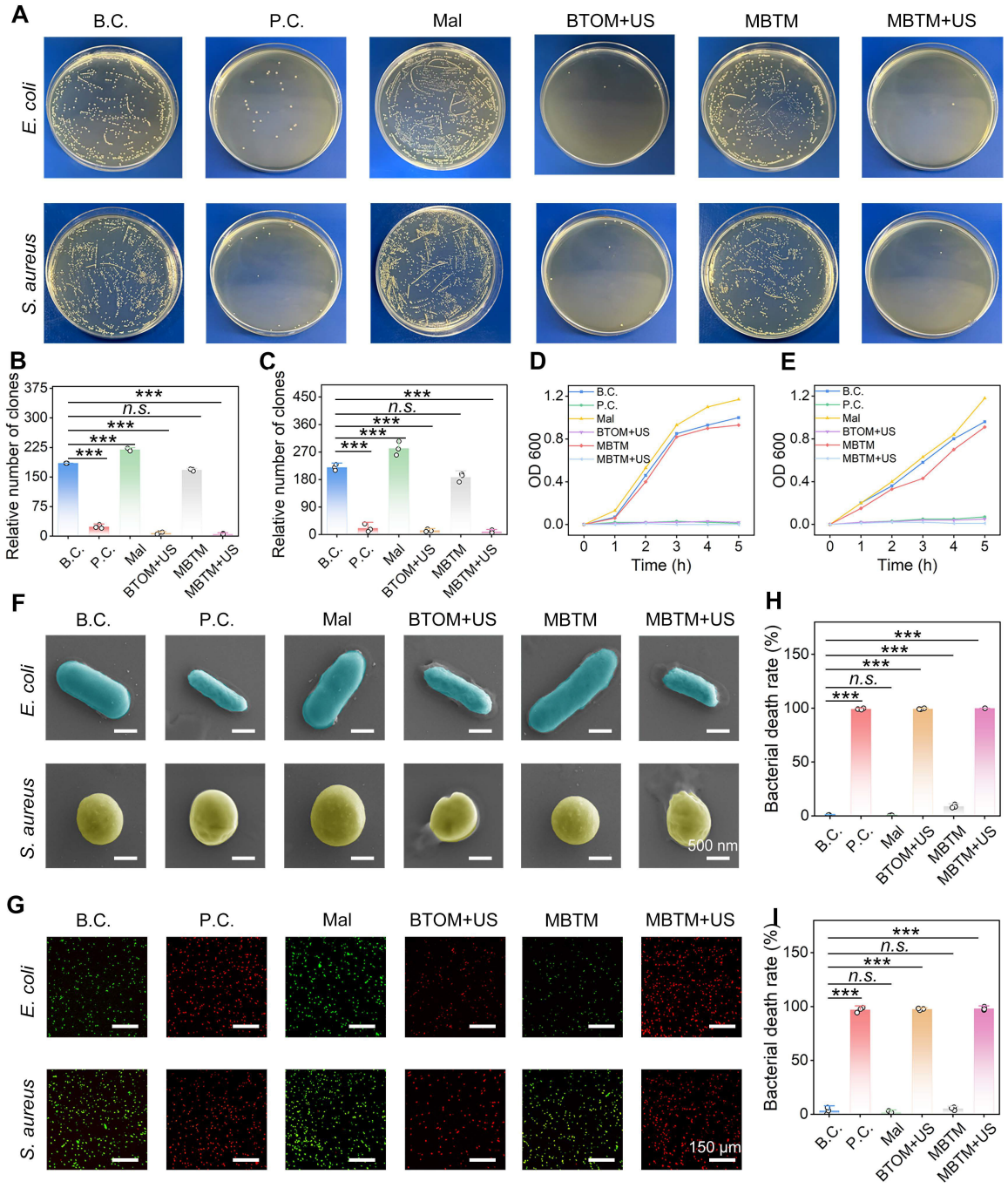


Figure 5. MBTM microneedle eliminated gram-positive and gram-negative bacterial infection. (A) Plate clone assay; (B) Relative clone number of *E. coli* (n = 3 biological replicates); (C) Relative clone number of *S. aureus* (n = 3 biological replicates); (D-E) Proliferation curves of *E. coli* and *S. aureus*, respectively; (F) Bacterial morphology observed by SEM. Scale bar: 500 nm; (G) Live/dead bacterial viability staining. Scale bar: 150 μm; (H-I) Bacterial death rate of *E. coli* and *S. aureus*, respectively (n = 3 biological replicates). All values are presented as mean ± SD. Statistical significance was assessed by one-way ANOVA. In inter-group comparisons, *n.s.* indicates no significance, ***$P < 0.001$.

In vivo promotion of infected wound repair by MBTM

As shown in Figure 6A, a full thickness skin defect model was established to evaluate the wound healing effect of MBTM microneedle. The wounds were 15 mm in diameter. Following *S. aureus* infection, the wounds were dressed with an MBTM microneedle and then subjected to ultrasound treatment. Animals were housed under standard conditions during the healing period. As shown in Figure 6B, these wounds healed within 18 days. In particular, MBTM+US group healed fastest among the five groups. Quantitative data on wound healing rate are provided in Figure 6C-D. More specifically, on Day 3, the wound healing rate was 17.4 ± 1.14% for B.C. group, 22.6 ± 1.82% for 3M® group, 24.7 ± 1.09% for BTOM+US group, 22.1 ± 1.60%

for MBTM group, and 30.9 ± 1.95% for MBTM+US group, respectively; that at Day 6 was 41.89 ± 1.56% for B.C. group, 50.16 ± 1.42% for 3M® group, 53.78 ± 0.79% for BTOM+US group, 48.08 ± 1.46% for MBTM group and 65.72 ± 1.86% for MBTM+US group, respectively. The MBTM+US group differed significantly from the B.C. group ($P < 0.05$). Thus, MBTM+US significantly accelerated the closure of infected wounds.

As shown in Figure 6E, neo-skin tissues were harvested for H&E staining analysis. At Day 6, the wounds were filled with granulation tissue, blood vessels, and inflammatory cells. Abundant granulation tissue was observed in the MBTM+US group, which was significantly more than that in the other groups. Granulation tissue not only fills the wound defect and provides nutrients and oxygen, but also facilitates re-epithelialization and confers antimicrobial defense. Early rapid granulation tissue formation is beneficial for wound healing [43]. At Day 18, intact keratinized epithelium was observed in all groups, indicating that the wound repair process was nearly complete. The MBTM+US group further exhibited denser collagen fibers, more mature keratinized epithelium, and newly formed hair follicles. These results demonstrated that MBTM+US exhibited the most favorable wound healing [44, 45]. In this study, the pro-regenerative effect of MBTM+US could be preliminarily attributed to its antibacterial properties, as demonstrated in Figure S10. Nevertheless, additional studies are required to clarify the other pro-regenerative effects of MBTM+US and the mechanisms involved.

MBTM activated complex pro-regeneration pathways

Histological staining analyses were conducted to investigate the mechanism by which MBTM+US promotes regeneration. Figure 7A and Figure 7D-E show the results of immunofluorescence (IF) staining images of ROS and Ki67. ROS is a key indicator of oxidative stress, and its downregulation typically promotes cell survival, whereas Ki67 is a widely recognized proliferation marker. Relative to the B.C. group, the MBTM+US group exhibited significantly reduced ROS levels and enhanced Ki67 expression ($P < 0.001$), suggesting that MBTM+US treatment attenuates oxidative damage while concurrently enhancing cellular proliferative activity. Figure 7B, Figure 7F-G and Figure S11 show the results of CD86 and CD206, which are canonical surface markers for pro-inflammatory M1 and anti-inflammatory M2 macrophages, respectively. Our results demonstrated that MBTM+US effectively induced M2 macrophage polarization, a phenotype known to orchestrate an immunosuppressive and tissue-reparative milieu that is conducive to skin wound healing. Furthermore, as shown in Figure 7C and Figure 7H-J, MBTM+US treatment also enhanced vascularization, as evidenced by CD31 expression, and promoted collagen remodeling, as indicated by Col-I and Col-III levels. Notably, the sample size for histological staining analysis was limited to 3, which may introduce a relatively high risk of bias. Accordingly, increasing the sample size would be necessary in future studies.

In conclusion, MBTM microneedles combined with ultrasound treatment accelerated infected wound healing through complex pathways, including alleviation of local infection and oxidative stress, modulation of the inflammatory microenvironment, and promotion of cell proliferation, angiogenesis, and collagen remodeling. In accordance with previous reports [46-48], this combined strategy does not merely serve as a simple additive antimicrobial approach, but rather orchestrates a coordinated regenerative cascade across successive healing stages. This stage-dependent synergy may help explain the superior healing outcomes observed compared with individual treatments, and highlights the potential of integrating physical stimulation with functional microneedle delivery for managing complex infected wounds.

Conclusions

This study first developed a MBTM microneedle platform incorporating Mal/BTO composite nanosheets, which enables piezocatalytic, biocompatible, and selective ROS therapy for infected wounds. BTO nanosheets were synthesized via a hydrothermal method and subsequently coated with a Mal layer through a solvothermal process. The obtained MBT nanosheets demonstrated good piezocatalytic activity for ROS generation. Meanwhile, they could be selectively internalized by both *S. aureus* and *E. coli* to upregulate their intracellular ROS levels, owing to the presence of Mal layer. MBT nanosheets were further modified by GelMA hydrogels to fabricate a MBTM microneedle. The results demonstrated that MBTM microneedles exhibited both biocompatibility and bioactivity to promote cell migration, as well as broad-spectrum antibacterial activity to inhibit bacterial survival and proliferation. Thus, MBTM successfully addressed the cytotoxicity concerns that accompany ROS-mediated antibacterial treatment. Under ultrasound stimulation, MBTM microneedles facilitated the healing of infected wounds via multifaceted mechanisms, including mitigation of local infection and oxidative stress, regulation of the inflammatory microenvironment, and enhancement of cell proliferation, angiogenesis, and collagen deposition. Notably, the overall

therapeutic performance of MBTM microneedles was superior to that of a commercial 3M® wound dressing. In conclusion, this study provides a potential microneedle platform that combines selective antibacterial activity and biocompatibility for infected wound management.

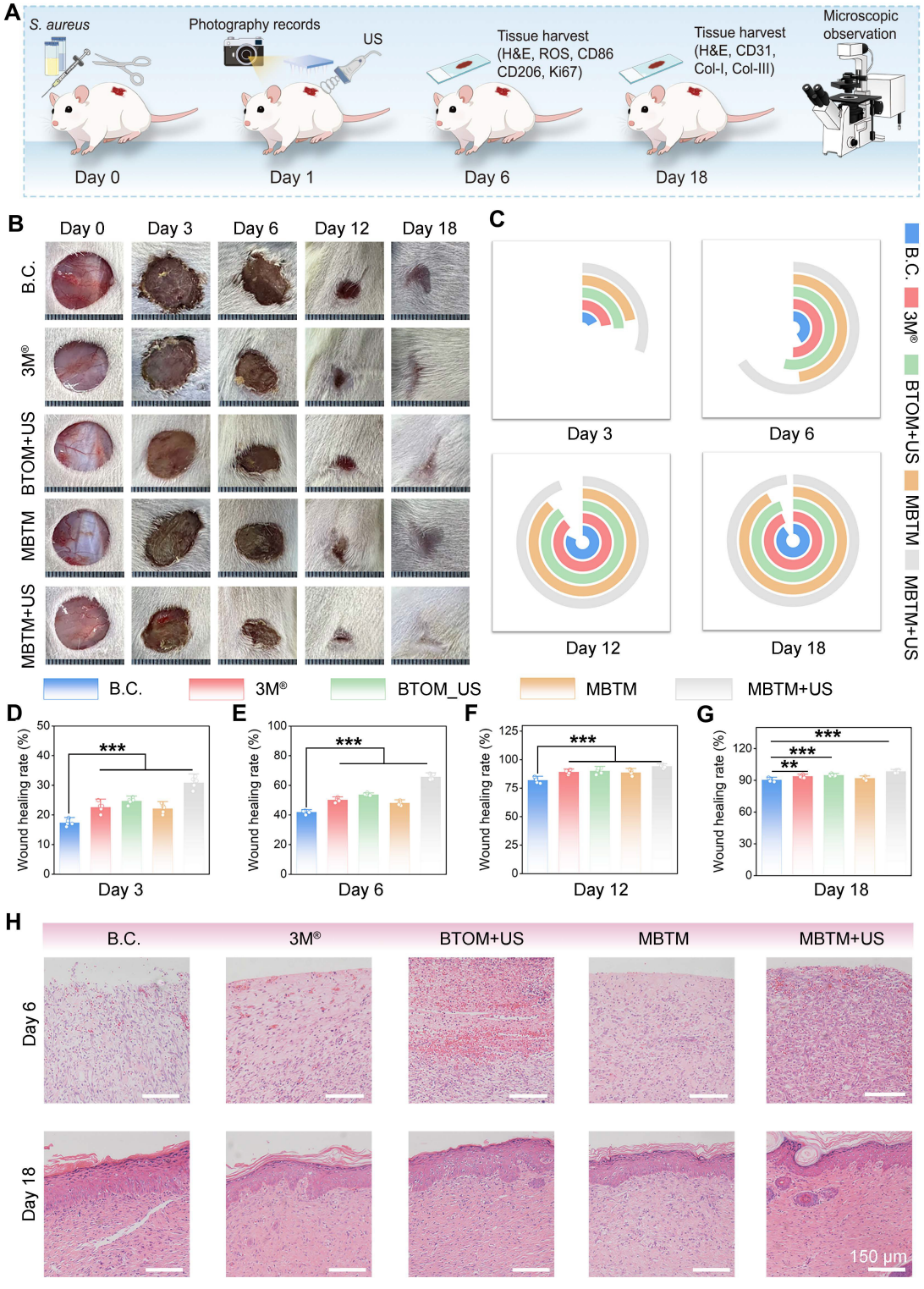


Figure. 6. *In vivo* acceleration of *S. aureus*-infected wound repair by MBTM microneedles. (A) Schematic illustration of the experimental workflow; (B-C) Representative photographs of skin wounds and the corresponding wound healing rate; (D-G) Quantitative results of wound healing rate at Day 3, Day 6, Day 12 and Day 18, respectively (n = 5 biological replicates); (H) H&E-stained sections of newly formed skin tissue. Scale bar: 150 μm. All values are presented as mean ± SD. Statistical significance was assessed by one-way ANOVA. In inter-group comparisons, $^{**}P < 0.01$, $^{***}P < 0.001$.

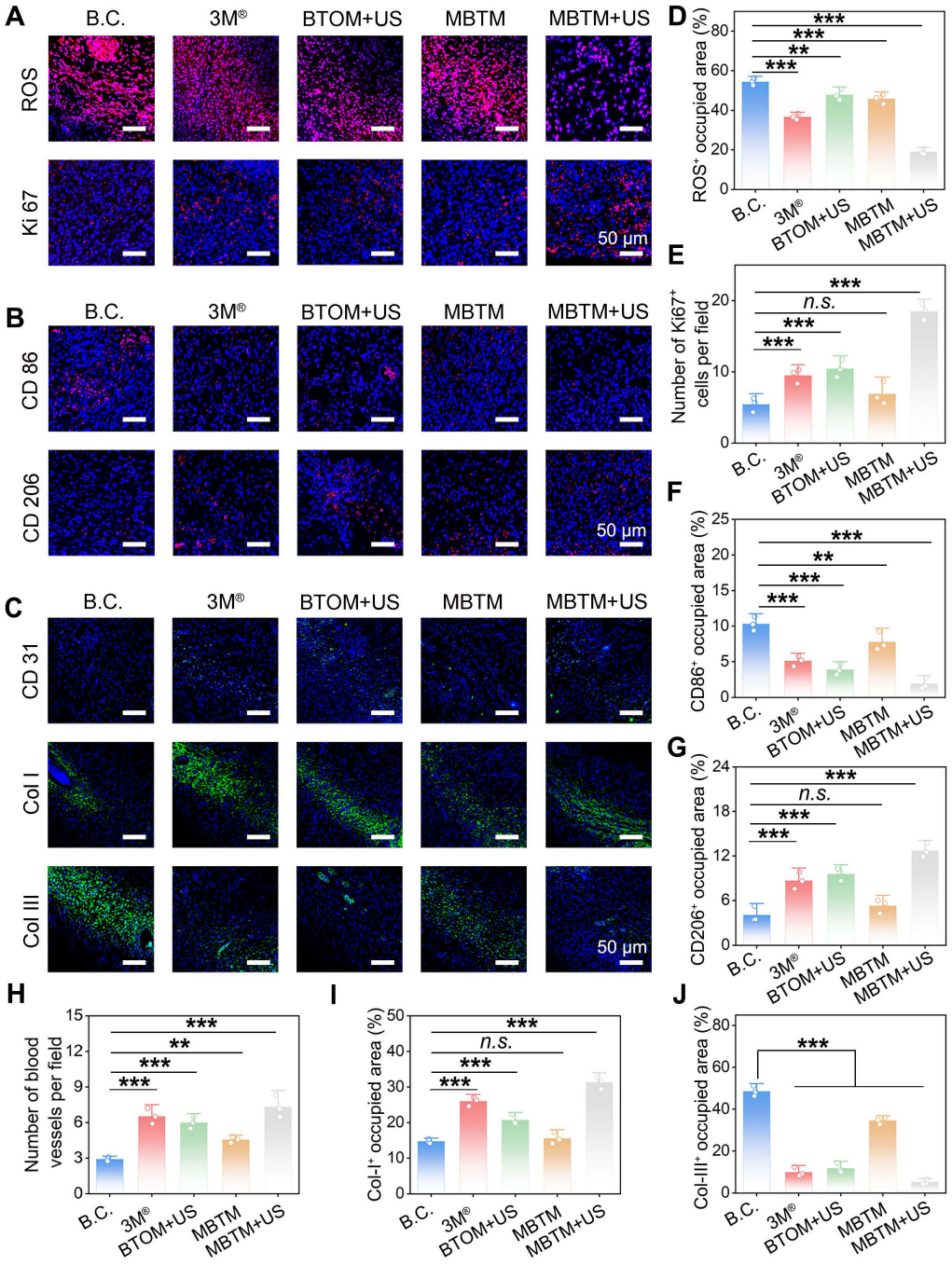


Figure 7. MBTM microneedle activated complex pro-regeneration pathways. (A) Immunofluorescence micrographs of ROS and Ki67 on Day 6. Scale bar: 50 μm; (B) Immunofluorescence micrographs of CD86 and CD206 on Day 6. Scale bar: 50 μm; (C) Immunofluorescence micrographs of CD31, Col-I and Col-III on Day 18. Scale bar: 50 μm; (D-E) Quantification of ROS and Ki67 (n = 3 biological replicates); (F-G) Quantification of CD86 and CD206 (n = 3 biological replicates); (H-J) Quantification of CD31, Col-I and Col-III (n = 3 biological replicates). All values are presented as mean ± SD. Statistical significance was assessed by one-way ANOVA. In inter-group comparisons, *n.s.* indicates no significance, ***$P < 0.001$.

Materials and Methods

Materials

$Ba(NO_3)_2$, $Ti(OC_4H_9)_4$, oleic acid, 1-butanol, and ethyl alcohol were purchased from Sinopharm Chemical Reagent Co., Ltd. (Shanghai, China). 4-O-(alpha-D-glucopyranosyl)-D-glucopyranose (Mal, CAS: 69-79-4, purity > 99.0%), methacrylic anhydride (MA), paraformaldehyde (PFA), and 2-hydroxy-4′-(2-hydroxyethoxy)-2-methylpropiophenone (I2959) were obtained from Macklin Chemical Regent Co., Ltd. (Shanghai, China). Dicyclohexyl carbodiimide (DCC), 4-dimethylaminopyridine (DMAP), and N,N-dimethylformamide (DMF) were purchased from Aladdin Scientific Co., Ltd. (Shanghai, China). A microneedle mold was obtained from Zhongding

Yuxuan New Material Technology Co., Ltd. (Hefei, China). L929 cells were generously provided as a gift by the Medical Research Center, Zhongnan Hospital of Wuhan University. Cell culture medium, trypsin, fetal bovine serum (FBS), and phosphate-buffered saline (PBS) were sourced from Thermo-Fisher Scientific Inc. (Shanghai, China). No further purification was performed on the other chemicals and reagents.

Preparation of BTO nanosheets

One mmol of $Ba(NO_3)_2$, and 12.5 mmol of NaOH were dissolved into 5 mL of deionized water, respectively. 1 mmol of $Ti(OC_4H_9)_4$ and 2.5 mL of oleic acid were added into 5 mL of 1-butanol. They were mixed together, and then transferred into a 100 mL stainless-steel autoclave. After reacted at 135 °C for at least 18 h, the autoclave was cooled to room temperature. BTO nanosheets were harvested by centrifugation (8000 rpm, 5 min), washed three times with ethanol, and then redispersed in DMF for subsequent experiments.

Preparation of MBT nanosheets

BTO were dispersed into DMF (2 mg/mL), and Mal were dissolved into DMF (20 mg/mL). Subsequently, BTO solution (20 mL) and Mal solution (20 mL) were combined with DCC (50 mg) and DMAP (6 mg), and the mixture was stirred continuously at 40 °C for 12 h. The products were sequentially rinsed with DMF and methanol for three times, and vacuum-dried to obtain MBT nanosheets.

Fabrication of MBT-laden MBTH hydrogels

GelMA was lab-customized following our previous protocols [49]. GelMA was dissolved into ultrapure water to prepare 15% (w/w) GelMA solution. As shown in **Table 1**, GelMA solution, MBT and I2959 were mechanically stirred with specific ratios. The resulting mixture was degassed by centrifugation, cast into molds, and irradiated with UV light for 300 s to initiate chemical cross-linking of the hydrogels. In this work, four composite hydrogel formulations were prepared and designated as MBTH-n (n = 0, 0.2, 0.5, and 0.8), corresponding to different MBT nanosheet contents.

Table 1. Designations, formulations, and fabrication conditions of MBTH hydrogels.

	15% GelMA (mL)	MBT (mg)	10% I2959 (μL)	Lamp power (W)	Curing duration (s)
MBTH-0	20	0	200	500	300
MBTH-0.2	20	6	200	500	300
MBTH-0.5	20	15	200	500	300
MBTH-0.8	20	24	200	500	300

Fabrication of bilayer microneedle patches

The bilayer MBTM microneedle patches were fabricated using a mold-casting technique. The base layer was composed of MBTH-0 hydrogels, while the tip layer was composed of MBTH-0.5 hydrogels. Detailed fabrication processes were illustrated in our previous report [50]. The patch dimensions are 14.5 × 14.5 mm, with 400 microneedles per patch, each measuring 600 μm in height and 250 μm in base diameter. Based on the concentration of the tip-loading solution and the volume of a single needle tip, the actual MBT loading per patch was calculated to be approximately 2.95 μg. To evaluate the performances of MBTM microneedles, this study also prepared the neat GelMA microneedles (coded as GM) and BTO-laden GelMA microneedles (coded as BTOM) as the controls.

Physicochemical characterizations

The morphology and elemental composition of the nanosheets were characterized by TEM (FEI Talos F200x, Thermo-Fisher, USA). FT-IR (Nicolet Is10, Thermo-Fisher, USA), XRD (D8 Advance, Bruker, Germany), and XPS (ESCALAB 250Xi, Thermo-Fisher, USA) were employed to analyze the chemical composition and lattice information of the nanosheets. FT-IR spectra were acquired in the wavenumber range of 400-4000 cm^{-1}. XRD data were collected with monochromatic Cu Kα radiation as the X-ray source; diffraction patterns were recorded from 10° to 80° (2θ) at a scanning rate of $10°\cdot min^{-1}$. The thermal stability of the nanosheets was assessed by thermogravimetric (TG) analysis on a STA 2500 Regulus instrument (Netzsch, Germany). TG measurements were carried out under a continuous N_2 flow at a heating rate of $10°\cdot min^{-1}$, and weight loss was monitored over 30-800 °C. Zeta potential was measured using a Zetasizer Pro (Malvern Instruments, UK) based on dynamic light scattering.

Piezoelectric tests

BTO and MBT nanosheets were homogeneously dispersed in ethanol to form a 5 mg/mL suspension. The resulting dispersion was uniformly drop-cast onto carbon sheet electrodes and air-dried to fabricate the working electrode. Electrochemical measurements were carried out in a three-electrode configuration consisting of a Hg/Hg_2Cl_2 reference electrode, a platinum counter electrode, and the as-prepared working electrode. A 5% sodium sulfate solution served as the electrolyte. EIS, LSV, and ultrasonic current density-time curve measurements were carried out at open-circuit potential. The piezoelectric properties of the nanosheets were further characterized by PFM (FX40, Park, China), where

amplitude and phase signals of the vertical piezoelectric response were acquired under an externally applied voltage of ± 10 V to generate piezoelectric mapping.

Evaluations of bacteria-specific internalization

Proliferative *E. coli* and *S. aureus* were cultured in Luria-Bertani liquid medium overnight. Bacterial suspension was collected by centrifugation, rinsed for three times, and resuspended into PBS with a concentration of 1.0×10^7 CFU. An aliquot of 20 μL of bacterial resuspension was co-incubated with BTO and MBT at 37 °C for 2 h. Bacteria were collected by centrifugation to obtain the bacterial pellet, primarily fixed with 2.5% glutaraldehyde at 4 °C for 4 h, washed with 0.1 M phosphate buffer, and then post-fixed with 1% osmium tetroxide at 4 °C for 2 h. Following dehydration in a graded ethanol series (50–100%) and subsequent substitution with 100% acetone, the samples were infiltrated and embedded using graded acetone: resin mixtures (1:1, 1:3, and pure resin), followed by polymerization at 60°C for 48 h. The embedded blocks were trimmed and sectioned into 60 - 90 nm ultrathin sections, which were collected on copper grids, stained with uranyl acetate and lead citrate, and finally observed and imaged under TEM.

MBT nanosheets were further labelled with FITC fluorescence for confocal observation of bacterial internalization. MBT was dissolved in carbonate buffer to ensure deprotonation of the hydroxyl groups on maltose. Subsequently, MBT and FITC solution were added into a light-shielded tube, and reacted with constant stirring in an ice bath for 12 h. The mass ratio of FITC to MBT was 1:50. After the reaction, the mixture was transferred into a dialysis bag and dialyzed against ultrapure water for 2 d.

FITC-labelled MBT nanosheets were added into a competitive co-culture system containing both bacteria and L929 cells. After 2 h of co-culturing, free MBT nanosheets were removed by centrifugation. The biodistribution of MBT nanosheets was visualized by laser confocal microscopy (Stellaris, Leica, Germany). Both bright-field and green fluorescence channels (excitation wavelength 488 nm, emission wavelength 525 nm) were detected. The focus and exposure parameters were adjusted to capture bright-field and fluorescence images across different fields of view, documenting the binding of FITC-MBT composites to bacterial surfaces, cellular internalization, and distribution patterns in the co-culture system.

Characterizations of ROS generation

The content of superoxide anion was measured by NBT assay. Specifically, 0.092 mg of NBT (750 μM) and 0.414 mg of methionine (130 mM) were added into 3 mL of PBS containing the nanosheets. Subsequently, the mixture was subjected to ultrasound treatment in a light-shielded environment. The ultrasound frequency was 1.0 MHz, the intensity was 1.2 W/cm², and the duty cycle was 50%. Each treatment lasted for 10 min. The solution was then centrifuged, and the absorption value of NBT was detected using an UV-Vis spectrophotometer. To comprehensively evaluate the superoxide anion-generating capability, additional experiments were also performed across a range of MBT concentrations (1, 2, 3, 4, 5, 10, and 20 mg/mL) and ultrasound treatment times (0, 5, 10, 15, 20, and 25 min).

The content of hydroxyl radical was measured by TMB assay. Specifically, 0.577 mg of TMB (0.8 mM) and 3.4 mg of H_2O_2 (10 mM) were added to 3 mL of PBS solution containing the nanosheets. Subsequently, the mixture was subjected to ultrasound treatment in a light-shielded environment. The solution was then centrifuged, and the absorption value at 652 nm was measured. To comprehensively evaluate the hydroxyl radical generation capability, additional experiments were also performed across a range of MBT concentrations (1, 2, 3, 4, 5, 10, and 20 mg/mL) and ultrasound treatment times (0, 5, 10, 15, 20, and 25 min).

The generation of hydroxyl radicals was further detected by EPR with DMPO as the spin-trapping agent. Briefly, a 10 mg aliquot of the sample was transferred into 2 mL of ultrapure water and initially dispersed with a vortex mixer. After 20 min of ultrasound treatment, the sample was centrifuged to collect the supernatant. 100 μL of the supernatant was mixed with 3 μL of DMPO, and the content of hydroxyl radical was immediately determined using EPR spectroscopy (ELEXSYS, BRUKER, Germany). Following the similar procedure, the content of superoxide anion was detected using methanol as the solvent.

Characterizations of composite hydrogels and microneedle patches

The hydrogels were freeze-dried for 48 h and then brittle-fractured using liquid nitrogen. The cross-sectional morphology and elemental distribution were analyzed using a SEM (Sigma 500, ZEISS, Germany) on the fractured sections. For mechanical tests, the hydrogels were cast into cylindrical samples prior to testing. The height and diameter of each sample were measured. Compressive tests were performed using a universal materials testing machine (CMT4000, SASTEST, China), with the compression fixture descending at 1 mm/min. Stress-strain curves were recorded, and the compressive modulus for each

group was calculated from the initial 10% slope of the curve. The compression curves of microneedles were also detected at dry condition. Water contact angle of the hydrogels was measured using a contact angle tester (SZ-CAMB1, SUNZERN, China). To evaluate the swelling behavior, hydrogel samples were cut into square specimens and vacuum-dried at 60 °C for 24 h to remove residual moisture. The initial dry mass was weighed on an analytical balance and denoted as W_0. The samples were then immersed in PBS. At preset time points, they were retrieved and gently blotted with filter paper to eliminate excess surface water. The wet mass was measured and recorded as W_t. Swelling ratios were calculated from three independent samples.

As previously reported[51], the *in vitro* release dynamics of the microneedles were evaluated using rhodamine B as a model compound. For the skin puncture test, 4-week-old female BALB/c-nu nude mice were employed. Prior to testing, animals received isoflurane inhalation anesthesia. The dorsal skin was harvested with sterile surgical instruments and immobilized on a flat plate. The microneedles were subsequently pressed against the excised skin for 1 min. Microneedle penetration was documented using a digital camera.

Biocompatibility evaluations

The microneedle patches were sterilized under UV irradiation. Mouse lung fibroblasts (L929) were seeded onto the upper surface of the samples and co-cultured for 48 h. Subsequently, 10% MTT reagent was added to each sample, followed by incubation for an additional 4 h. The culture medium was then completely removed, and dimethyl sulfoxide was added. After shaking in the dark for 10 min, 150 μL of the solution was transferred to a 96-well plate, and the absorbance at 490 nm was measured. According to the manufacturers' protocols, L929 cells adhered onto the microneedle patches were stained using a live/dead viability kit. An inverted fluorescence microscope was used for photo acquisition.

For the cell-migration assay, L929 cells that had adhered to the microneedle patches were harvested and then seeded into 6-well plates at a density of 6×10^5 cells per well. When cell confluence reached approximately 90%, the culture medium was removed, and a uniform scratch was created across the cell monolayer using a 200 μL pipette tip. The wells were washed three times with PBS, and then 1 mL of medium supplemented with 2% FBS was added to each well. The cells were cultured for an additional 24 h. The scratch width was recorded at regular time intervals using an inverted fluorescence microscope.

In vitro antibacterial evaluation

E. coli and *S. aureus* were selected as the model bacteria. MRSA was also used as a clinically relevant drug-resistant strain. The experimental groups included B.C., positive control (P.C., antibiotic), Mal, BTOM+US, MBTM, and MBTM+US. Bacteria were co-incubated with the materials and subjected to ultrasound treatment. The ultrasound frequency was 1.0 MHz, the intensity was 1.2 W/cm², and the duty cycle was 50%. Each treatment lasted for 10 min. According to our previous report, bacterial proliferation and viability were assessed using proliferation assays and colony-forming unit counting. Bacteria were stained with a live/dead bacterial staining kit and subsequently examined by SEM and confocal laser scanning microscopy to assess bacterial growth. For rescue assay, vitamin E was used as an anti-oxidant.

Wound healing assay

This study was performed in compliance with "Guiding Opinions on the Treatment of Animals (09/30/2006)" published by the Ministry of Science and Technology of the People's Republic of China and was approved by the Animal Ethics and Welfare Committee of Hubei University (Approval No. 20260038). Female Sprague-Dawley rats weighing 180 - 200 g were provided by the Laboratory Animal Center. Before surgery, all animals underwent a 7-day acclimation period in a specific-pathogen-free (SPF) environment. The rats were then randomly allocated to five separate groups: B.C., 3M® silver alginate dressing, BTOM+US, MBTM microneedles, and MBTM+US. Each group contained five biologically independent rats (n = 5 per group). Each rat was anesthetized via isoflurane inhalation, after which the dorsal fur was completely shaved with an electric shaver. Subsequently, a full-thickness skin defect with a diameter of 1.5 cm was created using sterile surgical instruments. Proliferating *S. aureu*s was then inoculated into the wound sites to establish an infected wound healing model. The materials were fixed onto the wound sites. The ultrasound frequency was 1.0 MHz, the intensity was 1.5 W/cm², and the duty cycle was 50%. During treatment, the ultrasound transducer was applied to the skin using gel as a coupling medium. Each treatment lasted for 10 min and was administered once daily.

Post-surgery, all rats were fed routinely for 18 days. No unexpected animal deaths occurred during the experiment. Wound-healing images were captured using a digital camera every 3 days. Wound closure was evaluated in all five rats per group. At the predetermined endpoint, all rats were sacrificed. For

histological analysis, three rats per group were randomly selected from the five rats using a random number generator, and the remaining two rats per group were not included in histological quantification. One wound tissue sample per selected rat was harvested and fixed in 4% PFA solution for 48 h. For each selected rat, three representative sections were used for histopathological staining and imaging, and the average value from the three sections was used as a single biological replicate. A series of histopathological staining assays were performed, including H&E and immunofluorescence (DCFH-DA, CD31, Ki67, CD86, CD206). Image acquisition was performed using a confocal laser scanning microscope. The percentage of positive area, defined as the ratio of positively stained area to the total field area, was quantified. All images were acquired with laser intensity, gain, and exposure parameters set using the blank control group as the reference, and the same parameters were applied to all other experimental groups. Image acquisition was completed within the same batch to avoid inter-operator variability. Thresholds were set using a fixed threshold method, and all quantitative analyses were performed independently by two researchers.

Statistical analysis

Quantitative results are expressed as the mean ± standard deviation (SD). For multiple-group comparisons, statistical significance was determined using a one-way analysis of variance (ANOVA) followed by Tukey's post hoc test. Statistical significance was defined as follows: *n.s.* indicates no significance, $^{*}P < 0.05$, $^{**}P < 0.01$, $^{***}P < 0.001$.

Supplementary Material

Supplementary figures.
https://www.thno.org/v17p0627s1.pdf

Acknowledgements

This work was supported by National Major Difficult Disease Clinical Collaboration Project between Traditional Chinese and Western Medicine (ZDYN-2024-A-18); Postdoctoral Fellowship Program of CPSF (GZC20241272); Hubei Provincial Postdoctoral Pioneer Talent Tracking Support Project (2025HBBSHXF048); Jichu-Zhongnan Joint Construction Project of Wuhan University (JCZN2025001); Open Research Fund of Hubei Key Laboratory of Urological Diseases (MNXTJB202401, MNXTJB202404). The authors acknowledge that Grammarly (AI-based writing assistance tool) was used for English language editing and proofreading of this manuscript. The authors remain fully responsible for the final content and accuracy of the manuscript.

Authorship contributions

They conducted the experiments and drafted the original manuscript. Wenwen Cheng compiled the data and generated the figures. Ye Yang, Zhengyao Zhang, Wang Wang provided assistance with data analysis and methodology. Weikang Hu and Weijun Liu contributed to funding acquisition, project administration and supervision. Zijian Wang conceptualized the project, led the funding acquisition, provided supervision, and revised the manuscript.

Data availability statement

The data supporting the results reported in this work are available from the corresponding author on reasonable request.

Competing Interests

The authors have declared that no competing interest exists.

References

[1] Zhao X, Xu H, Sun Y, Yang Y, Guo B. Self-Adaptive Wound Dressings for Wound Healing and Repair. Adv Mater. 2026; 38: e15854.
[2] Zhang SJ, Xu R, He SB, Sun R, Wang GN, Wei SY, et al. Nanozyme-driven multifunctional dressings: moving beyond enzyme-like catalysis in chronic wound treatment. Mil Med Res. 2025; 12: 27.
[3] Ge H, Wang M, Wei X, Chen XL, Wang X. Copper-Based Nanozymes: Potential Therapies for Infectious Wounds. Small. 2025; 21: e2407195.
[4] Zhou Q, Zhuang Y, Deng X, Jiang W, Wang X, Yuan C, et al. Hydrogel-Based ROS-Regulating Strategy: Reprogramming the Oxidative Stress Imbalance in Advanced Diabetic Wound Repair. Adv Mater. 2026; 38: e12719.
[5] Han C, Wang YQ, Gao SH, Wang T, Du HL, Long J, et al. High-entropy alloy Janus artificial enzymes for pH-gated sequential redox therapy of drug-resistant bacterial infection. Nat Commun. 2026; 17: 1266.
[6] Wang W, Huang L, Cheng W, Yang Y, Zhang Z, Hu W, et al. Rational design of Mn-MOF/MXene heterojunction microneedles for biocompatible ROS therapy of infected wounds. J Nanobiotechnol. 2026.
[7] You WJ, Cai ZC, Xiao F, Zhao JX, Wang GY, Wang W, et al. Biomolecular Microneedle Initiates Fe3O4/MXene Heterojunction-Mediated Nanozyme-Like Reactions and Bacterial Ferroptosis to Repair Diabetic Wounds. Adv Sci. 2025; 12: 2417314.
[8] Tao X, Fang ZJ, Shao R, Hu J, Cheng HY, Zhu SQ, et al. Covalent Organic Framework Nanohydrogel-Based Oxidase-Mimicking Nanozyme for Photocatalytic Antibacterial Therapy. Angew Chem Int Ed Engl. 2025; 64: e202513754.
[9] Chen ZG, Sang L, Bian DL, Liu YJ, Bai ZQ. Piezo-catalytic immunotherapy: mechanisms and feasibility in cancer treatment. Theranostics. 2025; 15: 6236–52.
[10] Musaie K, Abbaszadeh S, Marais K, Nosrati-Siahmazgi V, Rezaei S, Xiao B, et al. H2O2-Generating Advanced Nanomaterials for Cancer Treatment. Adv Funct Mater. 2025; 35: 2425866.
[11] Li M, Jafari H, Okoro OV, Nie L, Shavandi A. Nanozymes as catalysts for accelerated healing of diabetic wounds. Cell Biomater. 2025; 1: 100049.
[12] Shi S, Zhou HQ, Ming Y, Zhou X, Wu HB, Ren HP, et al. Bionic Cooling Skin for Infected Wound Healing. Nanomicro Lett. 2026; 18: 390.
[13] Xu W, Liu F, Wang L, Qin L, Guo J, Tan F, et al. Ultrasmall BaTiO(3) Nanoparticle-Based Piezoelectric Adhesive Bandage for Ultrasound-Driven, Drug-Free Antibacterial Wound Healing. Nano Lett. 2025; 25: 16894–904.
[14] Liu XY, Zhang HH, Chen LL, Zheng ZS, Li WW, Huang CY, et al. Advanced wound healing with Stimuli-Responsive nanozymes: mechanisms, design and applications. J Nanobiotechnol. 2025; 23: 479.
[15] Jia JL, Wang XS, Zhang T, Sun QX, Yang SD, Wu WN. Stimuli-responsive hydrogels based on cascade reactions: a novel strategy to promote the efficient repair of diabetic wounds. Theranostics. 2026; 16: 3105–35.
[16] Zhou W, Jiang X, Dong W, Xu X, Zhao P, Zhao Y, et al. Programmable hydrogel dressing for enhanced wound healing: Fuel-driven switchable antibacterial and antifouling properties. Cell Biomater. 2026; 2: 100300.

[17] Xiao Z, Cao J, Du T, Wang X, Du X. Bacterial ferroptosis-like death: Mechanisms and emerging therapeutic strategies. Coord Chem Rev. 2026; 557: 217758.
[18] Ning XH, Lee S, Wang ZR, Kim D, Stubblefield B, Gilbert E, et al. Maltodextrin-based imaging probes detect bacteria in vivo with high sensitivity and specificity. Nat Mater. 2011; 10: 602–7.
[19] Zlitni A, Gowrishankar G, Steinberg I, Haywood T, Gambhir SS. Maltotriose-based probes for fluorescence and photoacoustic imaging of bacterial infections. Nat Commun. 2020; 11: 1250.
[20] Ning X, Seo W, Lee S, Takemiya K, Rafi M, Feng X, et al. PET imaging of bacterial infections with fluorine-18-labeled maltohexaose. Angew Chem Int Ed Engl. 2014; 53: 14096–101.
[21] Gao Y, Wang H, Xue Y, Zhang Y, Huang S, Zhong Y, et al. A biodegradable nanoadjuvant resensitizes drug-resistant Klebsiella pneumoniae to β-lactam antibiotics. Nano Today. 2026; 69: 103077.
[22] Wang YX, Zhang MY, Yan ZZ, Ji SZ, Xiao SC, Gao J. Metal nanoparticle hybrid hydrogels: the state-of-the-art of combining hard and soft materials to promote wound healing. Theranostics. 2024; 14: 1534–60.
[23] Bigham A, Islami N, Khosravi A, Zarepour A, Iravani S, Zarrabi A. MOFs and MOF-Based Composites as Next-Generation Materials for Wound Healing and Dressings. Small. 2024; 20: e2311903.
[24] Gan Y, Liang B, Gong Y, Wu L, Li P, Gong C, et al. Mxene-based mild hyperthemia microneedle patch for diabetic wound healing. Chem Eng J. 2024; 481: 148592.
[25] Ding YJ, Wang JL, Li JY, Cheng Y, Zhou SY, Zhang YP, et al. Tβ4-Engineered ADSC Extracellular Vesicles Rescue Cell Senescence Through Separable Microneedle Patches for Diabetic Wound Healing. Adv Sci. 2025; 12: 2505009.
[26] Xiao J, Zhou Z, Zhong G, Xu T, Zhang X. Self-Sterilizing Microneedle Sensing Patches for Machine Learning-Enabled Wound pH Visual Monitoring. Adv Funct Mater. 2024; 34: 2315067.
[27] Yan J, Han Y, Xia S, Wang X, Zhang Y, Yu J, et al. Polymer Template Synthesis of Flexible BaTiO3 Crystal Nanofibers. Adv Funct Mater. 2019; 29: 1907919.
[28] Rodrigues J, Shimpi NG. High Performance-Low Cost-Chemiresitive BaTiO3 Nanospheres Based CO2 Gas Sensor for Air Quality Monitoring. ChemistrySelect. 2024; 9: e202401547.
[29] Lu S, Zhang S, Li L, Liu C, Li Z, Luo D. Piezoelectric effect-assisted Z-scheme heterojunction ZnIn2S4/BaTiO3 for improved photocatalytic reduction of CO2 to CO. Chem Eng J. 2024; 483: 149058.
[30] Zhao Z, Wang D, Gao R, Wen G, Feng M, Song G, et al. Magnetic-Field-Stimulated Efficient Photocatalytic N(2) Fixation over Defective BaTiO(3) Perovskites. Angew Chem Int Ed Engl. 2021; 60: 11910–8.
[31] Lu W, Pan X, Ong WL, Zeng K, Ho GW. Enhanced triboelectricity through visible-light-induced surface charges in BTO-polymer hybrid for coexistence solar-mechanical energy harvesting. Nano Energy. 2024; 128: 109867.
[32] Tang Q, Sun S, Wang P, Sun L, Wang Y, Zhang L, et al. Genetically Engineering Cell Membrane-Coated BTO Nanoparticles for MMP2-Activated Piezocatalysis-Immunotherapy. Adv Mater. 2023; 35: e2300964.
[33] Jing L, Zhuang F, Feng W, Huang H, Chen Y, Huang B. Doping-Engineered Piezoelectric Ultrathin Nanosheets for Synergistically Piezo-Chemocatalytic Antitumor and Antibacterial Therapies Against Cutaneous Melanoma. Small. 2024; 20: e2401171.
[34] Kong N, Zhang HJ, Feng C, Liu C, Xiao YF, Zhang XC, et al. Arsenene-mediated multiple independently targeted reactive oxygen species burst for cancer therapy. Nat Commun. 2021; 12: 4777.
[35] Hu X, Liu G, Wang L. Rational design strategies of antibacterial metal-organic frameworks: A review. Chem Eng J. 2026; 543: 178572.
[36] Chen P, He LG, Zhai H, Yan X, Luo KL, Yuan HQ, et al. Carbon dots in the generation of reactive oxygen species for antibacterial therapy: advances and challenges. Chem Commun (Camb). 2026; 62: 6046–65.
[37] Ouyang C, Shen F, Yu H, Wang L, Meng Y, Ni Z, et al. Nanoscale phase separation induced self-reinforced Janus hydrogel achieves robust adhesion under extreme acidity and anti-postoperative adhesions. J Colloid Interface Sci. 2026; 707: 139736.
[38] Zeng W, Zhang H, Deng Y, Jiang A, Bao X, Guo M, et al. Dual-response oxygen-generating MnO2 nanoparticles with polydopamine modification for combined photothermal-photodynamic therapy. Chem Eng J. 2020; 389: 124494.
[39] Cheng W, Wang W, Zhou Z, Yin H, Yang Y, Xiao F, et al. Defect engineering of zinc-based metal organic framework with enhanced ROS generation for antibacterial and wound healing applications. Nano Res. 2026; 19: 94908545.
[40] Xuan QZ, Cai JZ, Gao Y, Qiao XC, Jin TH, Peydayesh M, et al. Amyloid-Templated Ceria Nanozyme Reinforced Microneedle for Diabetic Wound Treatments. Adv Mater. 2025; 37: 2417774.
[41] Chen Z, Yu Y, Xiao X, Cheng W, Yang Y, Zhang Z, et al. Integrated O2 and H2 Gas Therapy via Microneedle-Assisted Photocatalytic Water Splitting for Accelerating Diabetic Full-Thickness Skin Wound Healing. Adv Sci. 2026: e77413.
[42] Jiang S, Wu J, Hang Y, Liu Q, Li D, Chen H, et al. Sustained release of a synthetic structurally-tailored glycopolymer modulates endothelial cells for enhanced endothelialization of materials. J Mat Chem B. 2019; 7: 4017–29.
[43] Yang W, Han D, Shi X, Li J, Li K, Xiang J, et al. Bioinspired Hydrogel Prepared by Core-Shell Nanofibers: Accelerating Wound Healing via Macrophage Polarization Modulation. Adv Funct Mater. 2026; 36: e24234.
[44] Zhao M, Xiang J, Meng Y, Sun H, Yang W, Li Z, et al. Astragalus Polysaccharide Hydrogels with Drug-Carrying Super Self-Assembly from Natural Herbs Promote Wound Healing. ACS Nano. 2025; 19: 21571–88.
[45] Li Q, Li B, Yang R, Chen X, Shang C, Feng G, et al. Photosynthesis pneumatic patch promoted deep-wound healing. Cell Biomater. 2025; 1: 100047.
[46] Xiong Y, Wu QP, Wang H, Shahbazi MA, Mi BB. ROS-responsive drug delivery systems for chronic wound healing: advances, challenges, and translational perspectives. Mil Med Res. 2026; 13: 100019.
[47] Wu QP, Xiong Y, Lu L, Wang H, Hu H, Shahbazi M, et al. Macrophage Membrane-Camouflaged Nanozyme Microneedles Restore Immunovascular Homeostasis Through SPP1-ApoE Signaling in Diabetic Wounds. Adv Healthc Mater. 2026; 15: e71456.
[48] Li S, Lu L, Xiong Y, Xiao J. Nanomedicine-based immunotherapy for tissue regeneration. Burns Trauma. 2025; 13: tkaf015.
[49] Chen ZS, Zhang YX, Feng KX, Hu T, Huang BH, Tang JL, et al. Facile fabrication of quaternized chitosan-incorporated biomolecular patches for non-compressive haemostasis and wound healing. Fundam Res. 2024; 4: 1243–53.
[50] Wang G, Wang W, Zhang Z, Wang X, Li S, Choy KL, et al. Engineered heterojunction microneedles initiate ROS-mediated "two-hit" mechanism for accelerating impaired wound healing in diabetes. Cell Biomater. 2026; 2: 100248.
[51] Zheng B, Li QY, Fang LP, Cai XL, Liu Y, Duo Y, et al. Microorganism microneedle micro-engine depth drug delivery. Nat Commun. 2024; 15: 8947.